Journal of Applied Physics

Versatile microparticle propulsion system by light-guided dielectrophoresis: Proposed method and theoretical calculation

Cite as: J. Appl. Phys. **130**, 054902 (2021); https://doi.org/10.1063/5.0052117
Submitted: 29 March 2021 . Accepted: 16 July 2021 . Published Online: 05 August 2021

Zexi Liang, and Donglei (Emma) Fan

Journal of Applied Physics ARTICLE scitation.org/journal/jap

Versatile microparticle propulsion system by light-guided dielectrophoresis: Proposed method and theoretical calculation

Cite as: J. Appl. Phys. **130**, 054902 (2021); doi: 10.1063/5.0052117
Submitted: 29 March 2021 · Accepted: 16 July 2021 ·
Published Online: 5 August 2021

Zexi Liang[1,a] and Donglei (Emma) Fan[1,2,b]

AFFILIATIONS

[1]Texas Materials Institute and Materials Science and Engineering Program, The University of Texas at Austin, Austin, Texas 78712, USA
[2]Walker Department of Mechanical Engineering, The University of Texas at Austin, Austin, Texas 78712, USA

[a]**E-mail:** liangphy92@utexas.edu
[b]**Author to whom correspondence should be addressed:** dfan@austin.utexas.edu

ABSTRACT

Developing materials for active matter that can efficiently respond to external stimuli with designed multifold mechanical motions remains a major challenge, and overcoming this will greatly propel the advancement of micromachines and microrobots toward unprecedented biomedical, electronic, and particle-separation applications. Here, we propose an innovative working mechanism that allows multifold-translational-motion control of semiconductor microentities by AC dielectrophoresis with simple visible-light stimulation. We study the dielectrophoresis forces on semiconducting particles of various geometries in aqueous suspension by modeling with the consideration of both the Maxwell–Wagner relaxation and the electrical-double-layer-charging effect. With the obtained understanding, we rationally design a manipulation system that can versatilely transport semiconductors and orient them toward desired directions simultaneously by tuning the light intensity in an electric field. This research could provide insights toward developing a new class of micromachines with rarely found control flexibility and precision and offer a new route toward separation and purification of optoelectric microparticles of different geometries.

INTRODUCTION

Future microrobots require a high degree of freedom in motion control to perform complex tasks by individuals or in a swarm. However, on a miniaturized scale, it is a daunting task to apply established actuation approaches used in macroscale robots to microrobots. Once the dimension of a system reduces to microscale, the complexity in integrating multiple functional components into one structure, resembling those in bulk machines, increases dramatically. However, the level of required forces to drive a microrobot is much reduced. The interactions that are insufficient for macroscale robots can become prominent for microrobots. Such forces include those generated by external magnetic,[1–12] electrical,[13–15] optical,[16,17] and acoustic fields,[18] as well as biochemical reactions,[19,20] which have successfully compelled versatile locomotion of micromotors. However, it remains arduous to control the manipulation of individual micromotors within a swarm in the same manipulation platform, not to mention to achieve it agilely and reconfigurably with desired orientations.[21]

Recently, we reported original working mechanisms that can rapidly switch the motion style and finely modulate the speed of both the mechanical rotation and alignment of a semiconductor microparticle in an AC electric field with simple visible light.[22,23] With experimental and theoretical simulation, we clarified that it is the visible-light-induced photoconductivity that modulates both the real and imaginary parts of the electric polarizability of a silicon nanorod at selected AC frequencies. As a result, the electromechanical phenomena such as the electrorotation and electroalignment can be modulated. The reconfigurable manipulations of the rotation and alignment of a micromotor are demonstrated with several potential implementations, including the differentiation of metallic/semiconductor microparticles[22] and communication of information via Morse-coded mechanical

motions.[23] Nevertheless, achieving versatile translocation of individual micromotors on a 2D surface in a swarm remains unknown and challenging. In addition, accomplishing this task may also suggest a new route for the separation and purification of photosensitive microparticles.

Previously, the combined electrophoresis (EP) and dielectrophoresis (DEP) have been exploited to compel longitudinal microparticles into linear transport with simultaneously controlled alignment.[24] In a DC electric field, electrophoresis is originated from the coulomb and electrokinetic interactions between a surface-charged particle and an external DC field, where the transport of the particle is either along or against the direction of the DC field, depending on the sign of its surface charge. In a non-uniform electric field (either DC or AC), a particle can experience a DEP force toward or opposite to the direction of the field gradient. The DEP force is governed by the real part of the electric polarizability of the particle, which is frequency dependent. In a uniform AC electric field, the DEP force becomes zero, but the interaction between the electric torque on the particle and the applied field can align a particle toward the field with controlled orientation. Thus, with a combined AC and DC electric field, a non-spherical particle can be manipulated on a 2D surface with transport and alignment controlled by the DC and AC fields, respectively. Here, this technique focuses on manipulating particles in an aqueous suspension where the DEP force has a prominent effect in an AC field while diminished in a DC field since a high-frequency field can effectively circumvent the countering polarization from mobile ions in an aqueous medium, i.e., the electric-double-layer effect. Therefore, the AC and DC fields result in distinct forces that can be utilized independently. While, in such a system, all particles of the same surface charges largely behave the same, they synchronously move and align in the same manner.

In this work, we propose an original manipulation method that can compel microparticles with multimode linear locomotion and simultaneously controlled alignment. The working mechanism is based on controlling interactions of light, electric fields, and semiconductors. The proposed mechanism is based on systematic calculation and simulation. The results provide a guidance on how to utilize light to modulate DEP forces applied to silicon microparticles of various geometries to select their different actuation modes. To be noticed, the proposed mechanism differs from the optoelectronic tweezers, although they both involve a photoresponsive semiconductor material with conductivity change upon local light illumination.

The optoelectronic tweezers utilize the light-induced photoconductivity change in the a:Si substrate to locally modulate the electrical field intensity and gradient for DEP generation.[25] Distinctly, our approach does not affect the distribution of the applied electrical field, but the polarizability of the particles is fine-tuned by light intensity. A successful implementation of the proposed approach could enable a new class of micromachines with rarely found individually controllable locomotion in a swarm. This work could also be applied toward the separation and purification of optoelectric microparticles with similar electric conductivities in dark but different geometries.

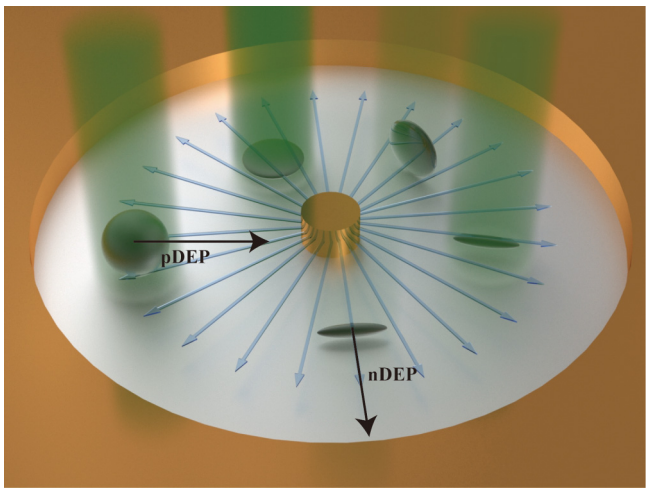

FIG. 1. Schematic of light-guided dielectrophoretic propulsion of silicon microparticles of different geometries and numerical simulation of electric-field distributions. For example, a pair of concentric circular microelectrodes with inner and outer electrodes generates a non-uniform AC field (as indicated by the blue arrows). Silicon particles of various geometries in de-ionized (DI) water are propelled by the light-controlled DEP forces. Light patterns projected onto individual particles excite photogenerated carriers and result in an increase in the conductivity of the particle so that both the direction and magnitude of the DEP forces can be tuned.

Design of concentric microelectrodes to generate a 1D radial electric field

We show one example on electrode design, i.e., concentric circular microelectrodes to generate the required non-uniform electric field for the DEP forces. This type of circular electrodes can be utilized for 1D manipulation along the radial direction (Fig. 1). The field can be generated via applying two AC signals with a 180° phase shift to the inner and outer electrodes, respectively. Any other electrode geometry with a non-zero field gradient can also be used for generating DEP forces.

Fundamentals of DEP based on the effective moment method

When a particle is subjected to an electric field, an electrical polarization is induced. The dipole moment is given by $\boldsymbol{p} = \alpha \boldsymbol{E}$, where α is the polarizability tensor of the particle. If the field is slightly non-uniform where a gradient exists, a force termed as a dielectrophoretic force is exerted on the particle, given by $\boldsymbol{F}_{DEP}(t) = \boldsymbol{p}(t) \cdot \nabla \mathbf{E}(t)$. For an AC electric field with a general expression of $\boldsymbol{E}(\boldsymbol{r}, t) = \boldsymbol{E}_0(\boldsymbol{r}, t) \cdot \exp(i\omega t)$, the DEP force is calculated as[26]

$$\boldsymbol{F}_{DEP}(t) = \mathrm{Re}\left[\underline{\boldsymbol{p}}\exp(i\omega t)\right] \cdot \nabla \mathrm{Re}\left[\underline{\boldsymbol{E}_0}\exp(\mathrm{i}\omega\mathrm{t})\right], \quad (1)$$

where $\underline{\boldsymbol{p}}$ and $\underline{E_0}$ are the phasor of the dipole moment and electric field, respectively. Since the AC electric-field period is generally much shorter than the time scale of the particle movement, what

can be observed is the time-averaged force ($\langle \boldsymbol{F}_{DEP}(t) \rangle$) exerted on a particle as follows:

$$\langle \boldsymbol{F}_{DEP}(t) \rangle = \frac{1}{2}\mathrm{Re}\left[\underline{\boldsymbol{p}} \cdot \nabla \underline{\boldsymbol{E}}_0^*\right] = \frac{1}{2}\mathrm{Re}(\underline{\alpha})\nabla \mathrm{E}_{\mathrm{rms}}^2, \tag{2}$$

where the asterisk refers to complex conjugation, $\underline{\alpha}$ is the complex polarizability tensor of the particle, and E_{rms} is the root mean square of the electric-field intensity. A positive DEP force (pDEP), which requires a positive real part of polarizability along the direction of the electrical field gradient, drags the particle toward the high-electric-field region. A negative DEP force (nDEP) occurs with a negative real-part polarizability and repels the particle away from the high-electric-field region. If the particle is non-spherical with anisotropy in the electric polarizability, an alignment torque is exerted on the particles, which is termed electro-alignment. For example, if a particle changes its orientation within the x–y plane, the alignment torque can be given by

$$\tau_{alignment} = -\frac{1}{2}E_0^2 \mathrm{Re}[\alpha_x - \alpha_y] \sin\theta \cos\theta \, \hat{z}, \tag{3}$$

where θ is the angle between the electric field and the x axis. When $\mathrm{Re}(\alpha_x) > \mathrm{Re}(\alpha_y)$, the particle's x axis orients toward the direction of the electric field; otherwise, the particle's y axis aligns in the direction of the electric field.

Here, we specifically study ellipsoid particles with a, b, c as half the length of the principal axes for two reasons: (1) an analytical solution exists for ellipsoid particles when it is subjected to a uniform electric field along the principal axes. (2) A model of ellipsoid particles can predict the behavior of microparticles of interest with shapes ranging from spheres and disks to rods, which are often made and used. In terms of the boundary value problem of an ellipsoid particle suspended in a uniform medium and a uniform electric field, an analytical solution exists. Suppose that the a, b, c axes of the ellipsoid particle are aligned along x, y, z axes of the coordinate system, respectively, the x component of the particle's electric polarization, for example, can be expressed as

$$p_x = \frac{4\pi abc}{3}\varepsilon_1 \frac{\underline{\varepsilon_2} - \underline{\varepsilon_1}}{\underline{\varepsilon_1} + (\underline{\varepsilon_2} - \underline{\varepsilon_1})L_x} E_x = \alpha_x E_x, \tag{4}$$

where ε_1 is the real permittivity of the medium; $\underline{\varepsilon_1}$, $\underline{\varepsilon_2}$ are the complex permittivity of the medium and the particle, respectively, given by $\underline{\varepsilon_i} = \varepsilon_i - \frac{i\sigma_i}{\omega}$; and L_x is the depolarization factor defined by the following elliptical integral:

$$L_x = \frac{abc}{2}\int_0^\infty \frac{ds}{(s+a^2)\sqrt{(s+a^2)(s+b^2)(s+c^2)}}.$$

Similarly, the expression for p_y and p_z can be obtained by the substitution of L_x and E_x in Eq. (4) with the corresponding terms for the respective direction. The Clausius–Mossotti factor K is defined as $\frac{\underline{\varepsilon_2}-\underline{\varepsilon_1}}{3\underline{\varepsilon_1}+3(\underline{\varepsilon_2}-\underline{\varepsilon_1})L_x}$, which governs both the frequency dependence and the geometry dependence of the polarization.

The frequency-dependent electric polarization of dielectric materials is known as dispersion. In optical frequencies, the Lorentz model can well explain the dispersion relation of dielectric materials that originate from multiple relaxation mechanisms. In most dielectrophoresis experiments, however, the frequency range of the alternating electric field is much lower and falls in the range of kHz to MHz, where the relaxation processes of atomic dipole, ionic polarization, and electronic polarization are not observed.[27] The only possible relaxation mechanism in these frequencies is the interface relaxation, also known as the Maxwell–Wagner interfacial polarization, which is originated from the discontinuity of the electrical properties at the interface between two mediums. Besides the effect of Maxwell–Wagner polarization that has been calculated in Eq. (4), due to the existence of ions in an aqueous solution, once the nanowire is polarized, the ions of opposite charges are spontaneously attracted toward the polarized surface to counter the surface charges and thus form charge electric layers, the so-called electrical double layers (EDLs). The behavior of the electrical double layer in an AC electric field could be very complex, and several models have been developed in order to predict the electrokinetic phenomena.[28–30] A full electrokinetic model that takes the induced-charge electroosmosis (ACEO) into consideration has been developed for particles with specific shapes.[31,32] Here, we utilize a simplified effective dipole moment model to represent the EDL effect, governed by an RC model[22] analysis. The effective dipole from EDL is generally opposite to the dipole from the Maxwell–Wagner relaxation with a certain phase lag and can be described by a Randles circuit as shown in Fig. 2(a). The equivalent circuit describes the electrokinetic process at the electrically polarized interfaces of the particle, where the EDL is forming to counter the surface charge from the polarized particle. The ionic resistance R_S connects in series with the double layer capacitance C_{EDL} and charge transfer resistance R_{CT} in parallel with C_{EDL}. However, in our discussion, the potential drop across the particle is insufficient for electrolysis so that no Faradaic reaction takes place, indicating an infinitely large R_{CT}. Thus, the circuit can be further simplified as an RC series circuit shown in Fig. 2(b), with a time constant τ_{RC}. The phase relation between the local electric field, the dipole moment from the Maxwell–Wagner polarization, and EDL is illustrated in Fig. 2(c), where the electric field is rotating counterclockwise with frequency ω, the dipole moment from the Maxwell–Wagner polarization ($\mathbf{p}_{MW}$) falls behind, and the dipole moment from EDL ($\mathbf{p}_{EDL}$) is further behind the $\mathbf{p}_{MW}$ with a phase lag of δ in the opposite direction. The effective dipole from the induced electrical double layer can be expressed as[22]

$$\mathrm{Im}(\mathrm{P_{EDL}}) = -\frac{[\mathrm{Re}(\mathrm{P_{MW}})\sin\delta + \mathrm{Im}(\mathrm{P_{MW}})\cos\delta]}{\sqrt{\omega^2\tau_{RC}^2 + 1}}, \tag{5}$$

$$\mathrm{Re}(\mathrm{P_{EDL}}) = -\frac{[\mathrm{Re}(\mathrm{P_{MW}})\cos\delta - \mathrm{Im}(\mathrm{P_{MW}})\sin\delta]}{\sqrt{\omega^2\tau_{RC}^2 + 1}}, \tag{6}$$

where τ_{RC} is the time constant for EDL charging and $\tan\delta = -\omega\tau_{RC}$ as the dielectric loss tangent (here, the minus sign shows that the phase of EDL falls behind the Maxwell–Wagner polarization). The value of τ_{RC} (2×10^{-5} s) is obtained from the fitting result of the previous experimental study in electro-rotation of silicon nanowires in the same de-ionized (DI) water medium.[22] We note

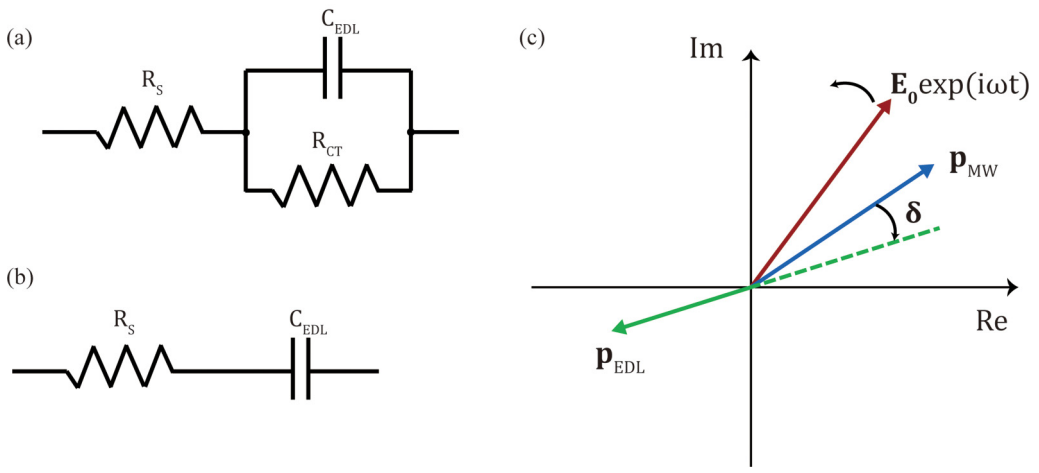

FIG. 2. Equivalent circuit at the interface of a polarized particle and the geometric representation of the phase relation of dipole moments in the complex plane. (a) The Randles circuit model describes the processes at the electrochemical interface, where R_S is the ionic resistance, C_{EDL} is the double layer capacitance, and R_{CT} is the charge transfer resistance. (b) Simplified circuit when there is no Faradaic reaction at the interface. (c) Geometric representation of the phase relation among electric fields, and dipole moments from the Maxwell–Wagner polarization and EDL.

that DI water has a finite conductivity of 4 μS/cm, indicating the existence of trace amount of ions so that the EDL can still form in such a medium. On the other hand, this simplified RC model for the EDL has several restrictions. The currently adopted value of τ_{RC} is obtained from experiments of silicon nanowires of 500 nm diameter in DI water of 4 μS/cm, where the thickness of the double layer is much smaller than the diameter of the nanowires so that the system lies in the thin double layer limit. The same limitation is required for our model. In the following, we discuss and calculate micrometer scale particles and in DI water.

Both the Maxwell–Wagner polarization and the electrical double layer contribute to the total electric dipole moment of the particles. Both the real and imaginary parts of the total dipole moment can be calculated accordingly. In this study, we select silicon as the material of the particle and de-ionized water as the suspension medium. Silicon is chosen due to the earthly abundance, high photoconductivity, and relevance to various practical applications. To understand the effect of light on the modulation of the DEP forces on Si microparticles via the tuning of their electric conductivities, we systematically sweep the electrical conductivity from 0.001 to 1 S/m in the calculation. The conductivity range is selected with the lower limit for the intrinsic silicon conductivity at room temperature, which can have a range depending on the fabrication process and the upper limit for an estimated magnitude of photoconductivity of microparticles under 1 W/cm^2 visible-light illumination.[22]

It is worth noting that the formation of EDL can modify the total external electric field that induces the electric polarization of the particle. To evaluate this effect, we introduce a correction factor β that represents the ratio between the applied external electric field (E_0) to the total field strength (E_{ext}) that polarizes the particle in the presence of EDL.

We consider the polarization linear to the applied field. We start with considering the case without an electrical double layer. The external field applied to the particle is $E_{ext} = E_0$, the actual field intensity inside the particle is E_{in} (for an ellipsoid particle, the field is uniform inside after polarization), and the depolarization field originated from the charge accumulation at interfaces due to polarization is $E_{depolar}$. The relation between these three field components is

$$E_{in} = E_{ext} + E_{depolar}. \tag{7}$$

Let $\lambda = E_{in}/E_{ext}$, this ratio is always a constant, as it is determined by the dielectric properties of both the particle and the surrounding medium, given by

$$E_{in} = \lambda E_{ext}, \tag{8}$$

$$E_{depolar} = (\lambda - 1)E_{ext}. \tag{9}$$

For ellipsoid particles, λ along the x axis can be calculated by

$$\lambda_x = \frac{1}{1 + \frac{\varepsilon_2 - \varepsilon_1}{\varepsilon_1} L_x}. \tag{10}$$

Now, we take the electrical double layer into consideration. The ions accumulated in the double layers at particle interfaces will induce an additional field that can affect the polarization of the particle. Now, the external field has two components: $E'_{ext} = E'_{EDL} + E_0$. The relation between the external field, the internal field, and the depolarization field still holds as $E'_{in} = \lambda_x E'_{ext}$ and $E'_{depolar} = (\lambda_x - 1)E'_{ext}$. We aim to solve the ratio between the actual external field intensity and the applied field intensity with

the double layer, which is

$$\beta_x = \frac{E'_{ext}}{E_{ext}} = \frac{E_0 + E'_{EDL}}{E_0}. \tag{11}$$

To calculate the electric field from the ions accumulated in the electrical double layers, we start with looking at its relation to the depolarization field $E'_{depolar}$. The depolarization field is originated by the accumulated charges at the particle–medium interfaces due to the electric polarization. When the particle is surrounded by an aqueous solution, a thin layer of counterions will be attracted toward the charged surface and a double layer is formed. As a result, the ions in the double layer will exert an additional electric field inside the particle in the opposite direction of the depolarization field. With the thin double layer assumption, the counterions are distributed in the region that is in close vicinity to the polarized surface; if the polarization charge on the particle surface is fully screened, the field from EDL should cancel out the depolarization field inside the particle. $E'_{EDL} \sim -E'_{depolar}$, which is the ideal case under a low strength DC field. In practice, however, the amount of charges in the double layer is always less than the polarization charge on the surface under an alternating field, as the double layer cannot reach equilibrium so that the counterions can only partially screen the surface charge with a phase lag. The frequency dependence of the charges in EDL and the polarization charge on the particle surface can be described by the equivalent circuit model discussed previously. As a result, the electric field from the charges in EDL and the depolarization field should follow the expression

$$E'_{EDL} = -E'_{depolar}\gamma, \tag{12}$$

where γ is the factor of the phase and magnitude between the surface charge and counterions. We inherit our previous RC circuit model to treat the frequency factor as $\gamma = \frac{\exp(i\delta)}{\sqrt{\omega^2\tau_{RC}^2+1}}$, the same with the phase relation between dipole moments in Eqs. (5) and (6). Combining Eqs. (9) and (12), the electric field from EDL can then be calculated as

$$E'_{EDL} = -(\lambda-1)(E_0 + E'_{EDL})\gamma = -\frac{(\lambda-1)E_0\gamma}{1+(\lambda-1)\gamma}. \tag{13}$$

Then, β can be calculated as

$$\beta = \frac{E_0 + E'_{EDL}}{E_0} = \frac{1}{1+(\lambda-1)\gamma}. \tag{14}$$

The dipole moment from the Maxwell–Wagner polarization with the modification of the influence of EDL can now be expressed as

$$p_{MWx} = \frac{4\pi abc}{3}\varepsilon_1 \frac{\underline{\varepsilon_2} - \underline{\varepsilon_1}}{\underline{\varepsilon_1} + (\underline{\varepsilon_2} - \underline{\varepsilon_1})L_x}\beta_x E_x = \alpha_x\beta_x E_x. \tag{15}$$

Here, we note that the correction factor β is a function of the dielectric properties of the particle and medium, the geometry of the particle, and the frequency of the field. We consider a spherical silicon particle with various conductivities in DI water, for example, and calculated the absolute value of β as a function of frequency as shown in Figs. S5 and S6 of the supplementary material. To be noticed, $|\beta|$ can be either greater or less than one. For $|\beta| > 1$, the EDL enhances the polarization and that happens when the polarizability of the particle is positive, and E'_{EDL} is in the same direction E_0. For $|\beta| < 1$, the EDL attenuates the polarization, as the polarizability of the particle is negative, and E'_{EDL} is in the opposite direction of E_0. However, when $|\beta| \gg 1$, the model becomes unphysical as the net charge density in EDL has an upper limitation, particularly for the DI water system proposed here. This also is in compound with the spatial distribution of charges in EDL from the surface. These indicate that Eq. (12) actually provides an estimation of the upper limit of the EDL effect, and when $|\beta| \gg 1$, the effect from EDL is much overestimated. Such overestimation occurs when $\lambda \to 0$ and $\gamma \to 1$ at the same time, corresponding to the case of highly conductive materials, e.g., metal and low-frequency field. Indeed, from Figs. S5 and S6 in the supplementary material, it is shown that only at low frequencies, i.e., below 10 kHz, and for particles with high electric conductivity, the issue of overestimation occurs. For frequencies above 200 kHz, the influence from EDL on the Maxwell–Wagner polarization is negligible (less than 0.1%).

Dependence of electric polarization on the AC frequency, geometry, and conductivity of Si particles

Next, we begin our investigation of the dependence of the Maxwell–Wagner polarization, which is the major contribution of the total electric polarization across all frequencies on the AC frequency, geometry, and conductivity of an Si particle. The real part of K can be written in the form of

$$\mathrm{Re(K)} = \frac{\varepsilon_2 - \varepsilon_1}{3\varepsilon_1 + 3(\varepsilon_2 - \varepsilon_1)L} + \frac{\dfrac{\sigma_2 - \sigma_1}{\sigma_1 + (\sigma_2 - \sigma_1)L}[\varepsilon_1 + (\varepsilon_2 - \varepsilon_1)L] - (\varepsilon_2 - \varepsilon_1)}{[\varepsilon_1 + (\varepsilon_2 - \varepsilon_1)L]\left(1 + \dfrac{[\varepsilon_1 + (\varepsilon_2 - \varepsilon_1)L]^2}{[\sigma_1 + (\sigma_2 - \sigma_1)L]^2}\omega^2\right)}. \tag{16}$$

By defining the Maxwell–Wagner charge relaxation time as $\tau_{MW} = \frac{\varepsilon_1 + (\varepsilon_2 - \varepsilon_1)L}{\sigma_1 + (\sigma_2 - \sigma_1)L}$, Eq. (6) can be written as

$$\mathrm{Re}(K) = \frac{\varepsilon_2 - \varepsilon_1}{3\varepsilon_1 + 3(\varepsilon_2 - \varepsilon_1)L} + \frac{(\sigma_2 - \sigma_1)\tau_{MW} - (\varepsilon_2 - \varepsilon_1)}{[\varepsilon_1 + (\varepsilon_2 - \varepsilon_1)L](1 + \tau_{MW}^2\omega^2)}. \tag{17}$$

The low-frequency limit of the Maxwell–Wagner polarization is $K = \frac{\sigma_2 - \sigma_1}{3\sigma_1 + 3(\sigma_2 - \sigma_1)L}$, and the high-frequency limit is $K = \frac{\varepsilon_2 - \varepsilon_1}{3\varepsilon_1 + 3(\varepsilon_2 - \varepsilon_1)L}$. For a silicon particle and DI water with $\sigma_2 - \sigma_1 > 0$ and $\varepsilon_2 - \varepsilon_1 < 0$, the Maxwell–Wagner polarization has a positive low-frequency limit and a negative high-frequency limit. There is always a crossover frequency ω_C that divides the positive and negative polarization region, regardless of the particle geometry. The crossover frequency ω_C at which $\mathrm{Re}(K) = 0$ can be

expressed as

$$\omega_C = \sqrt{\frac{\sigma_1 - \sigma_2}{\varepsilon_2 - \varepsilon_1}\frac{L\sigma_2 + (1-L)\sigma_1}{L\varepsilon_2 + (1-L)\varepsilon_1}}. \quad (18)$$

For a spheroid particle ($a = b$), $L_a = L_b = (1 - L_c)/2$. As the aspect ratio $\beta = c/a$ increases, L_c decreases and $L_{a,b}$ increases. For disk-like particles ($a = b$, c is small), $L_a = L_b \ll 1$ and $L_c \approx 1$. For spherical particles, $L_a = L_b = L_c = \frac{1}{3}$. For needle-like particles ($a = b$, c is large), $L_a = L_b \approx \frac{1}{2}$ and $L_c \ll 1$. The depolarization factor vs aspect ratio is shown in Fig. S1 of the supplementary material. Since $\sigma_2 > \sigma_1$ and $\varepsilon_2 < \varepsilon_1$, the crossover frequency increases with the depolarization factor L. In another words, a higher aspect ratio (c/a) leads to a lower crossover frequency along the major axis. Furthermore, L is bounded between 0 and 1, there naturally exist two limits of the crossover frequency, the upper limit is $\lim_{L\to 1}\omega_c = \sqrt{\frac{\sigma_1-\sigma_2}{\varepsilon_2-\varepsilon_1}\frac{\sigma_2}{\varepsilon_2}}$, and the lower limit is $\lim_{L\to 0}\omega_c = \sqrt{\frac{\sigma_1-\sigma_2}{\varepsilon_2-\varepsilon_1}\frac{\sigma_1}{\varepsilon_1}}$. Non-spherical particles have different depolarization factor L along different axes, and the corresponding crossover frequencies are different (as long as $\frac{\sigma_2}{\varepsilon_2} \neq \frac{\sigma_1}{\varepsilon_1}$). Thus, there exist differences among the crossover frequencies along different axes, and as a result, the particle will favor different alignment orientations at different frequencies. For spheroid particles, the crossover frequency along the major axis (the longest principal axis) ω_{C1} is lower than that along the minor axis (the shortest principal axis) ω_{c2}. When $\omega < \omega_{C1} < \omega_{C2}$, the particle aligns with the major axis in parallel to the field. When $\omega_{C1} < \omega < \omega_{C2}$, the particle aligns to the orientation that the minor axis is parallel to the field. When $\omega_{C1} < \omega_{C2} < \omega$, the particle favors the orientation that the major axis is parallel to the field again. Different crossover frequencies along different axes enable a distinct approach to control the particle orientation by tuning the AC field frequency, and a wide frequency window between ω_{C1} and ω_{C2} is preferred. From Eq. (18), it can be found that the depolarization factor L plays the role as a weight coefficient in the expression. A higher aspect ratio of the particle leads to a larger discrepancy in the depolarization factor along major and minor axes and results in a wider frequency window between the two crossover frequencies. Finally, with the value of ε_1, ε_2 and σ_1 fixed, increasing the particle conductivity σ_2 (upon light exposure) can effectively increase the low-frequency limit of K, as well as the crossover frequency ω_C. For non-spherical particles, the width of the frequency window between ω_{C1} and ω_{C2} also increases with the particle conductivity σ_2, as the difference between $\frac{\sigma_2}{\varepsilon_2}$ and $\frac{\sigma_1}{\varepsilon_1}$ increases with σ_2.

Besides the Maxwell–Wagner polarization, the electrical double layer is also frequency dependent with a different relaxation time τ_{RC}. From Eqs. (5) and (6), it can be found that, at low frequencies ($\omega_{\tau_{RC}} \ll 1$), both real part and imaginary part of the total polarization along any axes almost vanish at the low-frequency limit due to the EDL screening, while at high frequencies, they are asymptotic to the Maxwell–Wagner polarization as the EDL effect gradually fades away with the increase of the AC frequency. With consideration of the EDL effect, we separately calculate the polarization components of the Maxwell–Wagner polarization and EDL as well as the total polarization of three representative particles as shown in Figs. S2–S4 of the supplementary material. In this system, the relaxation time of EDL ($\tau_{RC} = 2 \times 10^{-5}$ s) is always longer than the Maxwell–Wagner charge relaxation time τ_{MW} within the considered range of particle conductivity and regardless of the particle geometry. The crossover frequency determined from the real-part Maxwell–Wagner polarization is almost identical to the crossover frequency of the total polarization as shown in Figs. S2–S4 of the supplementary material.

Numerical results and analysis

With the above analytical discussion of the frequency, geometry, and conductivity dependence of polarization, we then conducted a numerical investigation for a set of spheroid particles. First, oblate spheroid silicon particles ($a = b > c$) are studied, including one sphere ($a = b = c = 5\,\mu$m) and another five spheroids with monotonically reduced aspect ratio $\beta = c/a$ from 0.8 to 0.1 with the half-axis length a and b fixed at 5 μm. Both polarization at a low conductivity ($\sigma_{Si} = 0.001$ S/m) and a high conductivity ($\sigma_{Si} = 1$ S/m) are calculated to demonstrate the effect of photoconductivity upon light exposure. The polarizability is calculated by using the model discussed above by considering both the Maxwell–Wagner relaxation and the electrical-double-layer effect.

As shown in Figs. 3(b) and 3(c), the electric polarizability along the major axes (the longest principal axes, which are a axis and b axis in this case) always vanishes at the low-frequency limit due to the EDL screening, while at the high-frequency limit, it levels off to a negative value as discussed in the previous section. The magnitude of the electric polarizability decreases when the spheroid shrinks in the c axis, which agrees with Eq. (3), which indicates that the electric polarization is directly proportional to the volume of a particle. By comparing the electric polarizability at both low and high electric conductivities controlled by light illumination, it can be readily found that the electric conductivity plays an immense role in governing the frequency-dependent electric polarization. First, by increasing the electric conductivity, the magnitude of the peak of the positive electric polarizability can be augmented by several times depending on the particle geometry, and the peak of the positive polarization can extend to a broad range of frequencies into a plateau, which is a result of $\frac{1}{\tau_{RC}} \ll \frac{1}{\tau_{MW}}$. By tuning the electric conductivity from 0.001 to 1 S/m, for the spherical particle (#1), the maximum positive polarizability can be magnified by around three times, while for the disk-like oblate spheroid (#6) with an aspect ratio (c/a) of 0.1, the magnification is more than 11 times (Table I). Thus, with the reduction of the dimension along the c axis, the increase in the electric polarization by the light-enhanced electric conductivity becomes more effective. For the negative polarizability, at the low electric conductivity, the crossover frequency occurs at around 200 kHz, while at the high electric conductivity controlled by light, the switching frequency shifts to above 100 MHz, which is already beyond the commonly used AC-frequency range for electrokinetics. As a result, below 200 kHz, the positive electric polarization can be much improved by the increase in the electric conductivity, and the positive DEP force can be amplified several times. At the same condition, when it is above 200 kHz, the sign of the electric polarization, as well as the DEP

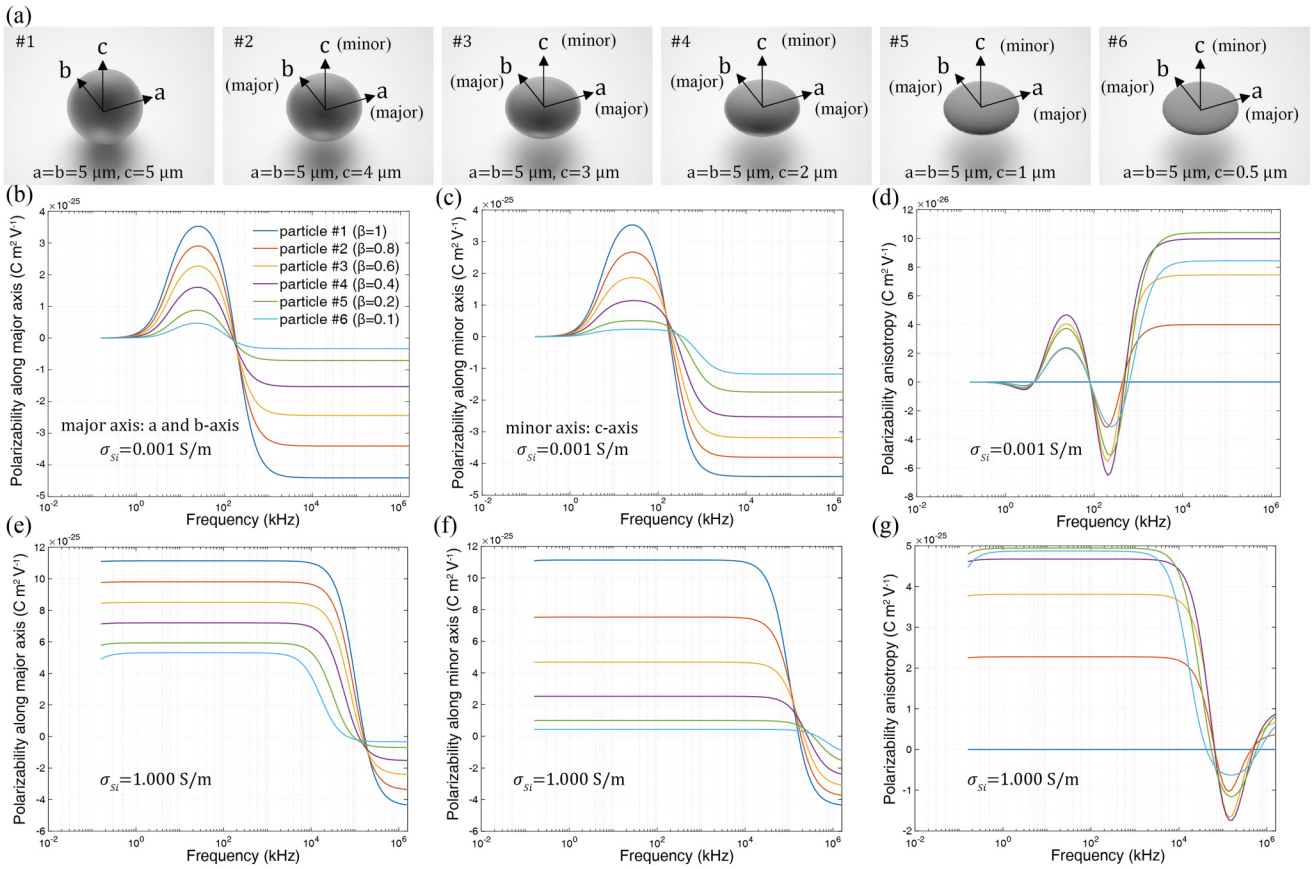

FIG. 3. Calculation of the electric polarizability and anisotropy (difference between polarizabilities along the major axis and the minor axis) of various oblate spheroid Si particles with different electric conductivities in the medium of de-ionized water with a conductivity of 4 μS/cm. (a) Six oblate spheroid particles in the simulation. (b)–(d) The electric polarizability along the major axes (a and b axes), the minor axis (c axis), and the anisotropy of the oblate spheroid particles with a low conductivity of 0.001 S/m and (e)–(g) a high conductivity of 1 S/m.

force, can be switched from negative to positive by increasing the conductivity.

Furthermore, when a particle changes the geometry from spherical and oblate spherical to disk as shown in Fig. 3(a), the directional anisotropy of electric polarizability emerges and the electric polarizability along the c axis differs from that of a axis for a particle of either a low [Fig. 3(d)] or high electric conductivity [Fig. 3(g)]. As the anisotropy of the electric polarizability along different axes emerges, the orientation of the particle should be considered since the total electrical potential energy is different along different orientations. For an oblate spheroid, it either orients with a and b axes or c axis along the direction of the electric field depending on which polarizability has a greater real-part value as shown in Eq. (3). We calculate the anisotropy of the electric polarizability, given by $\mathrm{Re}[\alpha_a - \alpha_c]$, of all the six shapes [Fig. 3(a)] for a particle of either a low [Fig. 3(d)] or high electric conductivity [Fig. 3(g)]. It is found that at a low electric conductivity, all the oblate spheroidal particles orient toward the a axis (or b axis) along the electric-field direction below ~77 kHz, switch to the c-axis alignment with the electric field between 77 and around 550 kHz (slightly different for different geometries), and then switch back to the a-axis alignment even at higher frequencies. At high conductivity, all of the oblate spheroidal particles align with one of its major axes orienting along the electric-field direction below 60 MHz, switch to the minor-axis alignment in the range of ~60 to ~100 MHz, and then switch back to the major-axis alignment even at higher frequencies. The sphere [#1 in Fig. 3(a)] does not show electric anisotropy and alignment effect, but even a minor shape change can result in such an effect [oblates #2–6 in Fig. 3(a)]. In addition, by comparing the sign of the anisotropy of the electric polarizability between 77 and 550 kHz for a particle of low [Fig. 3(d)] and high conductivities [Fig. 3(g)], it is clear that the orientation of oblate particles can be facilely switched between the two alignment states by tuning the electric conductivity with light. More will be discussed later.

Another type of special geometry of interest is the prolate spheroids ($a = b < c$). Here, we studied six prolate spheroids with an aspect ratio $\frac{c}{a}$ that range from 1 to 10, where the half length a and b

TABLE I. The maximum positive polarizability of all particles along the major axis at low and high conductivities and the magnification factors.

Oblate particle number (#)	1	2	3	4	5	6
Aspect ratio (c/a)	1	0.8	0.6	0.4	0.2	0.1
Maximum positive polarizability at low conductivity ($Cm^2\ V^{-1}$)	3.59×10^{-25}	2.96×10^{-25}	2.31×10^{-25}	1.63×10^{-25}	8.84×10^{-26}	4.69×10^{-26}
Maximum positive polarizability at high conductivity ($Cm^2\ V^{-1}$)	1.11×10^{-24}	9.81×10^{-25}	8.49×10^{-25}	7.20×10^{-25}	5.94×10^{-25}	5.31×10^{-25}
Magnification	3.1×	3.3×	3.7×	4.4×	6.7×	11.3×
Prolate particle number (#)	**7**	**8**	**9**	**10**	**11**	
Aspect ratio (c/a)	1.25	1.67	2.5	5	10	
Maximum positive polarizability at low conductivity ($Cm^2\ V^{-1}$)	2.43×10^{-25}	1.46×10^{-25}	6.99×10^{-26}	1.92×10^{-26}	$5.01 \times 10^{-27.}$	
Maximum positive polarizability at high conductivity ($Cm^2\ V^{-1}$)	8.60×10^{-25}	6.36×10^{-25}	4.39×10^{-25}	2.64×10^{-25}	1.79×10^{-25}	
Magnification	3.5×	4.4×	6.6×	13.8×	35.7×	

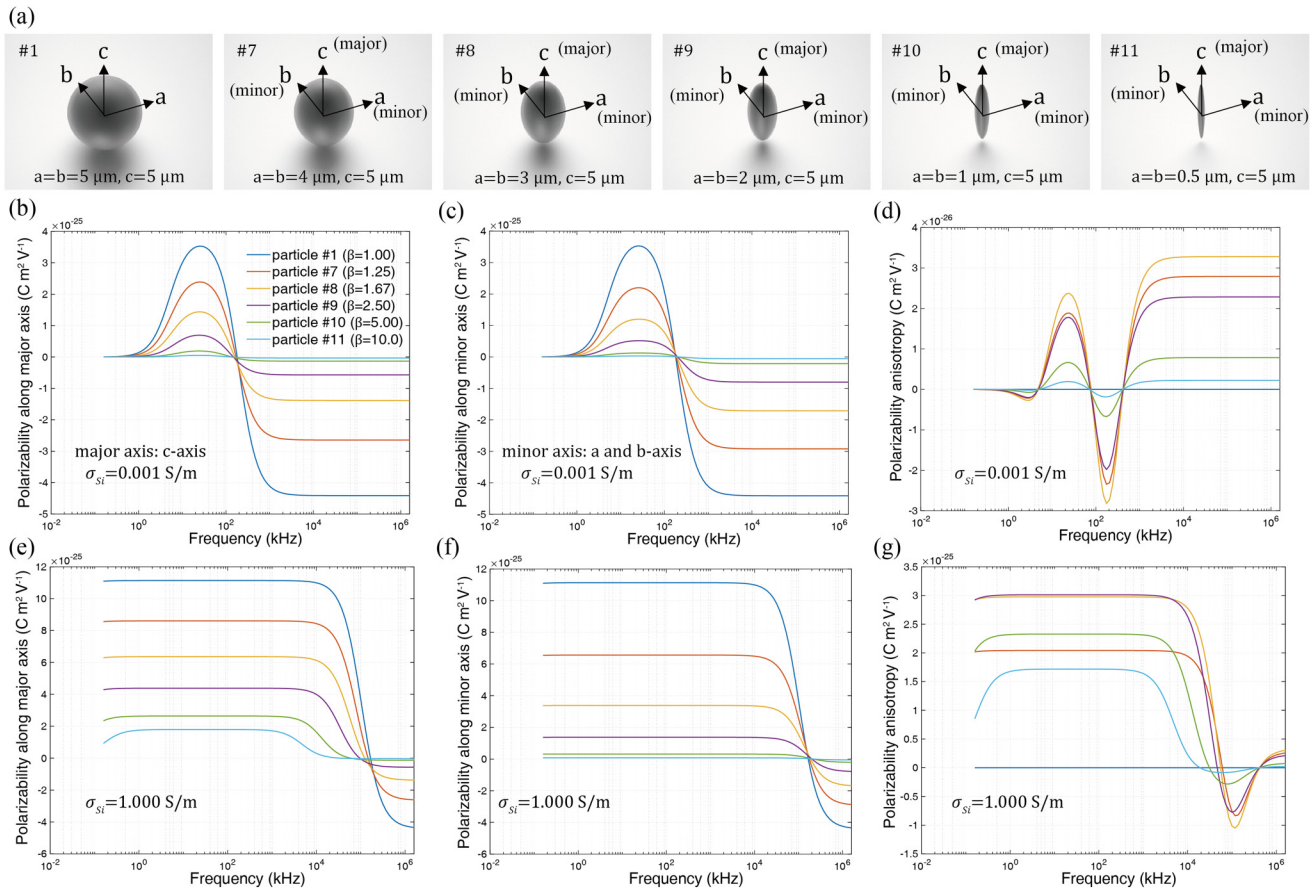

FIG. 4. Calculation of electric polarizability and electric anisotropy of various prolate spheroidal silicon particles with different electric conductivities suspended in de-ionized water with a conductivity of 4 μS/cm. (a) Diagrams of six prolate spheroidal particles. Electric polarizability along the (b) major axes (c axis) and (c) minor axes (a and b axes), and (d) the electric anisotropy of the six prolate spheroid particles of a low electric conductivity of 0.001 S/m and (e)–(g) a high conductivity of 1 S/m.

range from 5 to 0.5 μm and $c = 5\,\mu$m. As shown in Figs. 4(a)–4(f), the prolate spheroid polarizability spectrum is generally similar to that of the oblate spheroid, with moderate differences in amplitude and frequency. Particularly, it is found that the amplification of the positive electric polarizability along the major axis (c axis) between the low and high conductivities increases with the aspect ratio $\frac{c}{a}$. The needle-like prolate particle (#11), for example, has an aspect ratio of 10, and its polarizability along the c axis amplifies more than 35 times as the electric conductivity increases from 0.001 to 1 S/m by light, while with the same change in electric conductivity, the electric polarizability of a spherical particle (#1) can only be enhanced by around three times [Figs. 4(b) and 4(e), Table I]. Thus, the prolate spheroids are better shapes for obtaining a large range of light-tunable DEP forces with high sensitivity to electric conductivity.

The above discussion summarizes the systematic study of the frequency, geometry, and conductivity dependence of electric polarizabilities of silicon spheroid particles in DI water from both numerical results and analytical discussion. The obtained understanding is essential to realize the function-oriented design of microparticles for efficient light-reconfigurable manipulation and applications.

Light-stimulated transport of microparticles with simultaneously controlled alignment

The obtained results of the dependence of the electric polarizability of Si microparticles on the geometry, AC frequency, and electric conductivity are critical for us to design innovative systems for light-stimulated versatile transport of microparticles with simultaneously controlled alignment. For simplicity, we first consider the scenario that the electric-field gradient is parallel to the electric-field direction. Such an electric-field distribution can be implemented by applying an AC voltage onto two concentric circular electrodes as shown in Fig. 1. Both the electric field and the gradient of the electric field are radial, pointing toward the center of the inner electrode (to be quantitatively discussed later). We select particle #1 (sphere), #6 (oblate spheroid, disk-like, aspect ratio 0.1), and #11 (prolate spheroid, needle-like, aspect ratio 10) as three representative geometries and demonstrate versatile manipulation in both transport and alignment tuned by the frequency and photoconductivity modulation.

Due to the geometric symmetry, a spherical particle experiences zero alignment torque in an AC electric field, and the polarizability is isotropic. Within a concentric electric field, there are only three possible modes of motion for the spherical particles: (1) moving toward the center, (2) moving away from the center, and (3) no motion. It is possible to switch the motion modes by just controlling the light intensity at a given AC frequency, a result of the tuning of the photoconductivity of the silicon particles. Here, in addition to the light-controlled photoconductivity, there could be additional electric conductivity from doping and thermal excitation. For simplicity, we consider that Si is undoped, and the photoconductivity is the dominant source of electric conductivity due to its change of many orders of magnitude. We calculate the electric polarizability of the spherical particle #1 by varying the electric conductivities from 0.001 to 1 S/m

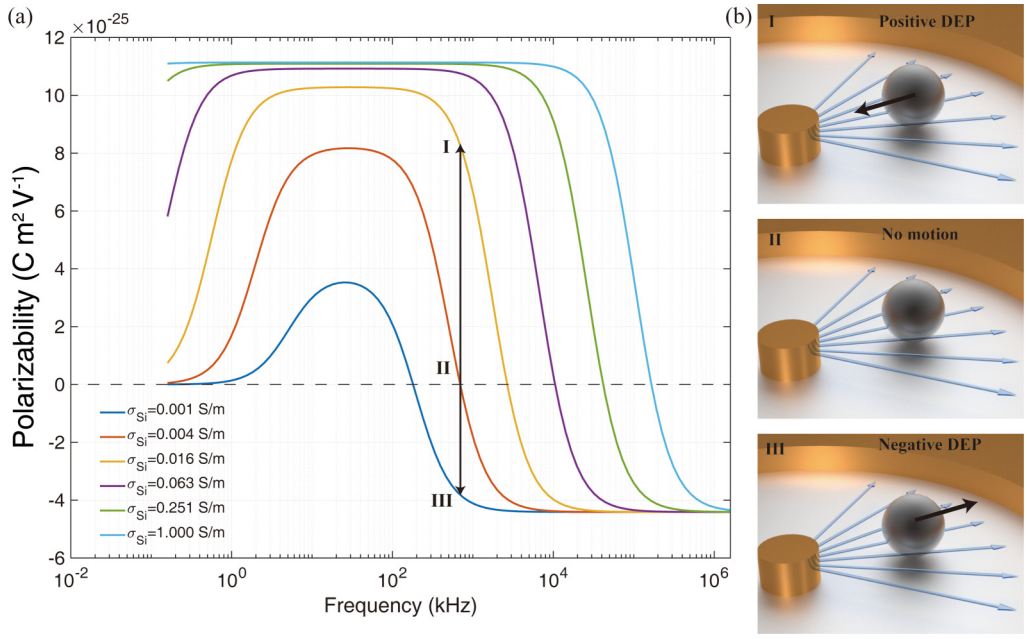

FIG. 5. Calculation of the electric polarizability of the spherical particle (#1). (a) Electric polarizability of a spherical particle vs AC frequency with different electric conductivities. At 700 kHz, I, II, and III show three possible motion modes with positive, zero, and negative DEP forces, respectively. (b) Corresponding diagrams of the three motion modes.

as shown in Fig. 5(a). The AC frequency is selected to be 700 kHz, where a transition of the polarizability from negative to positive occurs. A base light intensity is defined at which the particle's electric conductivity equals 0.004 S/m. At this condition, the real-part electric polarizability equals zero, and the particle remains stationary as indicated as point II in Figs. 5(a) and 5(c). If the light intensity increases higher than this base value, a positive DEP force is triggered, and the particle transports toward the center electrode [point I in Figs. 5(a) and 5(b)]. If the light intensity decreases below this base value, a negative DEP force is produced, and the particle moves outward from the center [point III in Figs. 5(a) and 5(d)].

For the oblate particle #6 (disk-like, aspect ratio 0.1), there are more possible modes of motion. To depict the general behavior, we first calculate the real-part polarizability along the major axes (a and b axes) and minor axis (c axis) as well as the polarizability anisotropy ($\mathrm{Re}[\alpha_a - \alpha_c]$) at a series of electric conductivities from 1 to 0.001 S/m as shown in Figs. 6(a)–6(c). With the obtained results, we select an AC frequency at 1 MHz, where we can obtain five distinct motion modes as summarized in Fig. 6(d) and Table II.

By utilizing the same approach, we analyze the electric polarizability, anisotropy, and motion modes of the prolate particle #11 (needle-like, aspect ratio 10) as shown in Figs. 7(a)–7(d) and Table III. For the prolate particle #11, a, b axes are the minor axes and c axis is the major axis. The anisotropy is defined as $\mathrm{Re}[\alpha_c - \alpha_a]$. The selected AC frequency is 2 MHz, at which the maximum number of motion modes occurs.

In summary, we demonstrate that for either the prolate or oblate spheroid particles, by selecting proper AC frequencies, one can rationally select and switch the translocation direction and alignment of a particle among five possible modes by simply modulating the photoconductivity. Two orientations either alignment along the semi-major or the semi-minor axis with the electric field can be obtained. Within each orientation, the DEP force can be finely tuned from a negative value to a positive value.

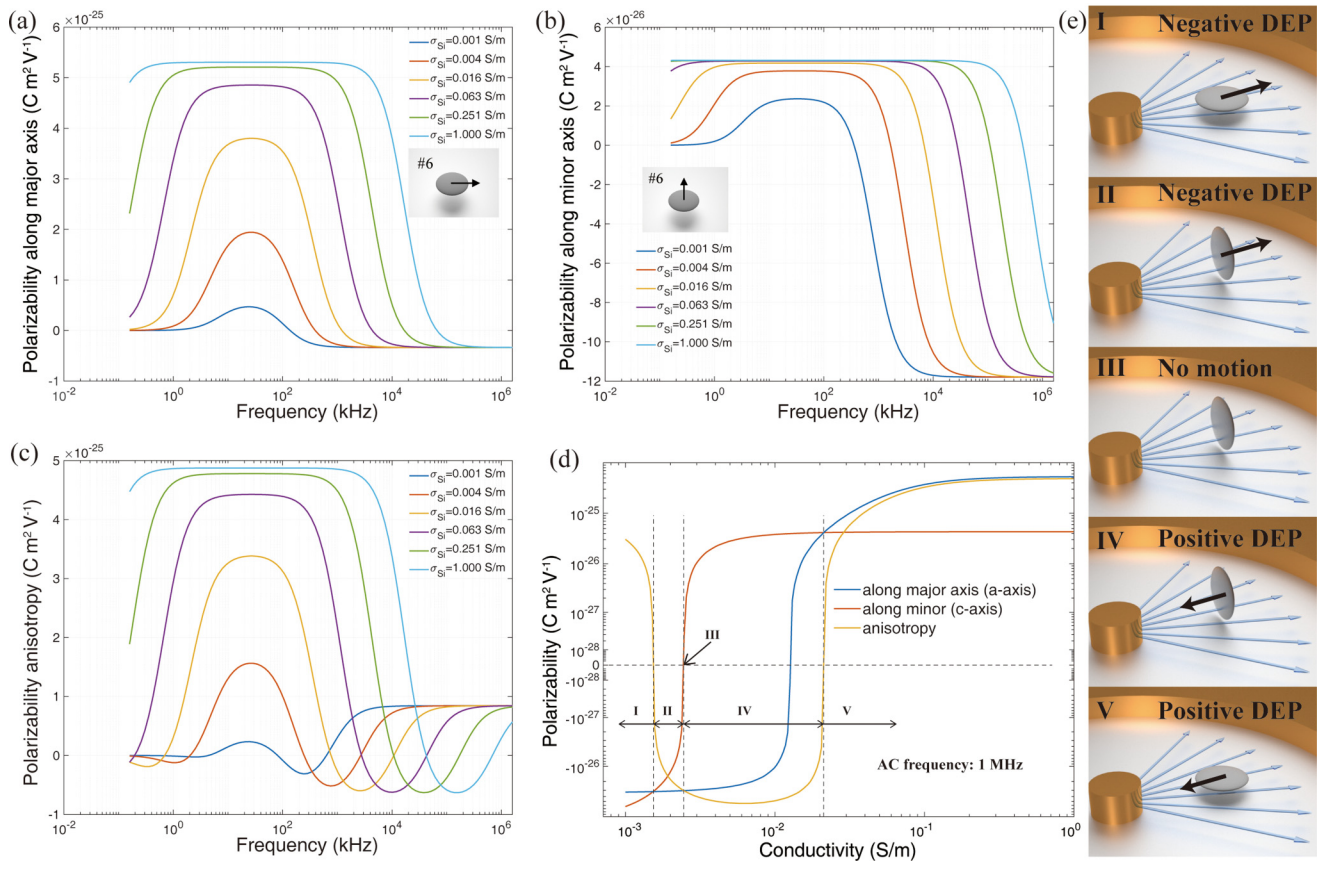

FIG. 6. Calculation of the electric polarizability of the oblate spheroid particle (#6, disk-like, aspect ratio 0.1). Electric polarizability of the particle along (a) the major axis and (b) the minor axis vs AC frequency with different electric conductivities (inset: diagram of the polarization direction). (c) Electric polarizability anisotropy between the major-axis and minor-axis polarizabilities. (d) Electric polarizability and anisotropy as a function of electric conductivity at 1 MHz. (e) Diagrams of the five inter-switchable motion modes.

TABLE II. Five inter-switchable motion modes of the oblate silicon particle (#6, disk-like, aspect ratio 0.1) with tunable electric conductivity by light in an electric field at 1 MHz.

Motion modes	I	II	III	IV	V
Conductivity (S/m)	<0.0015	0.0015–0.0024	~0.0024	0.0024–0.0219	>0.0219
Orientation along the E-field	Major axis	Minor axis	Minor axis	Minor axis	Major axis
Sign of a DEP force	Negative (−)	Negative (−)	Zero	Positive (+)	Positive (+)

DISCUSSION

In this work, we conducted a theoretical investigation on the tunable polarization of semiconductor microparticles under various light illumination and electric-field frequencies. The model we applied is based on the Maxwell–Wagner polarization at the particle–medium interface as well as the electrical-double-layer effect at the charged surfaces. The description of the Maxwell–Wagner polarization is analytical for the spheroid particles, while the model for the EDL is a RC model. In our model, the EDL is represented by an effective dipole moment in the opposite direction to the dipole from the Maxwell–Wagner polarization, which has proved its effectiveness in understanding experimental results in electrorotation and electroalignment in previously reported works.[22,23] Note that this model cannot predict the effect when the particle size is small enough to be comparable with the EDL thickness. In this work, we only consider the particle above the micrometer scale as the particle size is much larger than the electrical double layer thickness, i.e., a thin double layer approximation. A more sophisticated model can assist to understand a case when the size of a particle is

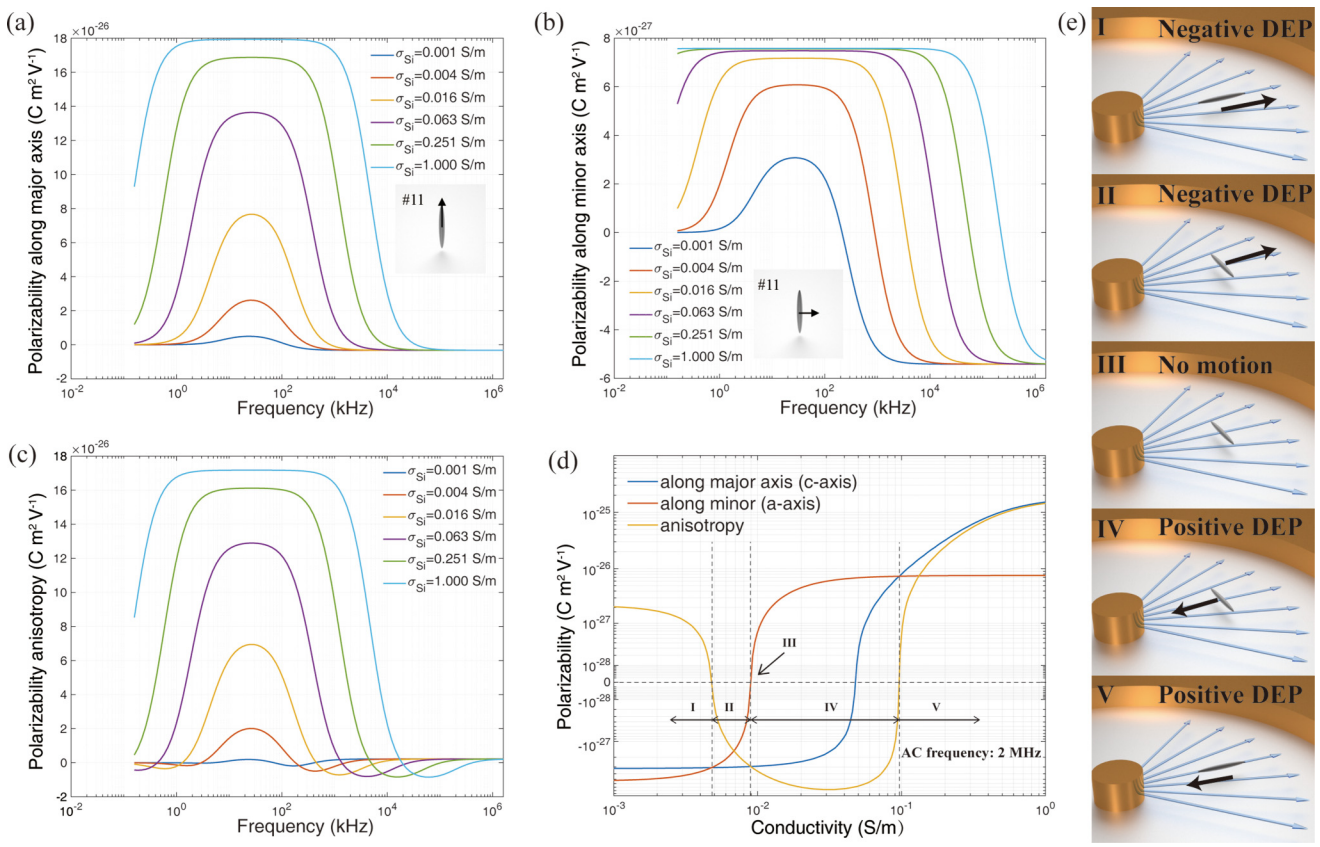

FIG. 7. Calculation of the electric polarizability of the prolate spheroid particle (#11, needle-like, aspect ratio 10). Electric polarizability of the particle along (a) the major axis and (b) the minor axis vs AC frequency with different electric conductivities (inset: diagram of the polarization direction). (c) Electric polarizability anisotropy between the major-axis and minor-axis polarizabilities. (d) Electric polarizability and anisotropy as a function of electric conductivity at 2 MHz. (e) Diagrams of the five inter-switchable motion modes.

TABLE III. Five inter-switchable motion modes of the prolate silicon particle (#11, needle-like, aspect ratio 10) with tunable electric conductivity by light in an electric field at 2 MHz.

Motion modes	I	II	III	IV	V
Conductivity (S/m)	<0.0024	0.0024–0.0045	~0.0045	0.0045–0.0437	>0.0437
Orientation along the E-field	Major axis	Minor axis	Minor axis	Minor axis	Major axis
Sign of a DEP force	Negative	Negative	Zero	Positive	Positive

comparable to electric double by coupling the ion transfer, electrostatic (quasi-static), and hydrodynamics (osmosis flow) simultaneously.[29,30,33] Also, as shown by a recent experiment that for particles with a size comparable to the EDL thickness, the Maxwell–Wagner polarization can be much overwhelmed by the space charge from the electrical double layer.[34]

In this work, we presented a theoretical investigation. It is desirable to further study the proposed light-controlled DEP manipulation to observe possible unforeseen efforts and unveil the potential limit. Here, we would like to point out the potential challenges that could arise in the experimental study. In this theoretical study, we considered an ideal 2D planar electric field and omitted all the possible effects from the specific design of electrodes. With practically fabricated microelectrodes, the electric field can have a non-ideal distribution in 3D at their edges that should be considered in experimental testing. When using thin film microelectrodes for electric manipulation, AC electroosmosis (ACEO) flow could be induced around the microelectrodes when applying an AC voltage at frequencies below tens of kHz. This could disturb the motion of the particles near the microelectrodes. Such ACEO flows can be suppressed by choosing a suspension medium with low electric conductivity and apply a high-frequency AC field. Moreover, the electrically polarized microparticles near the thin film metallic microelectrode could experience an attractive dipole–dipole interaction originated from the induced charges. To minimize such an interaction, the particles under investigation should be manipulated sufficiently away from the electrodes. The properties of Si microparticles that can vary with different fabrication processes should be considered as well, including the size, geometry, doping level, and surface conditions. The size may affect the EDL formation as previously mentioned. The geometry of particles will be influential to the light absorption at different wavelengths. Both doping level and surface oxidation will impact electric properties of the particle, deviating them from those of bulk silicon.

Here, we only presented an example of electrode design, i.e., circular microelectrodes. The same working principle could be extended to 2D and 3D manipulations by utilizing strategically designed microelectrodes to generate the required field gradient in three dimensions. For instance, multipole electrodes that are symmetrically arranged circularly could be applied to generate desired in-plane field gradient in both x and y directions, simply by adjusting the electrical potential applied on each of the microelectrode pads. By increasing the number of microelectrodes, fine control of the field gradient can be realized with the assistance of electrostatic simulation. Introducing the same electrode array on the top of the experimental cell, spaced by a thin separation layer, the electrical potential in 3D can be obtained, modulated, so does the field gradient. As a result, we expect the same working principle being applicable for 3D manipulation.

In terms of applications, in addition to micromachines, we envision that our work can add a new strategy to the current DEP-based cell/particle sorting techniques in continuous flow. For instance, controlling the orientation of non-spherical particles can change the drag coefficient for DEP-enabled particle sorting by geometry. Furthermore, if the particles are photo-responsive, a digital light projection system with a real-time image analysis will be able to generate and project dynamic light patterns and realize the modulation of each particle's conductivity and movement both simultaneously and independently.

CONCLUSION

In this work, we propose a new and versatile working mechanism that could be applied for developing an array of semiconductor-based light-controlled dielectrophoresis manipulation systems. The electrical property of a semiconductor micromotor can be controlled by external light stimuli and is exhibited as tunable mechanical motions in an external AC electric field. Systematic investigation of the polarization behavior of semiconductor particles has been conducted, focusing on the dependence on geometry, AC frequency, and electric conductivity. The selection and switching of modes of mechanical motion with only light modulated electric conductivity has been shown on spherical, oblate, and prolate particles.

In summary, this work could be particularly interesting for applications related to the remote and independent control of translocation of micromotors (or robots), such as the delivery of cargos to live cells in a biological study. It also could be utilized as a general platform that coordinates activities of micromotor swarms by large light patterns for a collaborative task force. Furthermore, it may be exploited for the applications of particle sorting based on geometry and photo-responsiveness.

SUPPLEMENTARY MATERIAL

See the supplementary material for the separated components of dipole moments from the Maxwell–Wagner polarization and the electrical double layer charging.

ACKNOWLEDGMENTS

We are grateful for the support of the National Science Foundation (NSF) via the CAREER Award (Grant No. CMMI 1150767 and intern supplement) and NSF research grants

(Nos. 1710922 and 1930649), the support of the Welch Foundation (Grant No. F-1734), and the University Graduate Continuing Fellowships to Z.L. (The University of Texas at Austin, 2019).

DATA AVAILABILITY

The data that support the findings of this study are available from the corresponding author upon reasonable request.

REFERENCES

[1]Z. Wu, J. Troll, H.-H. Jeong, Q. Wei, M. Stang, F. Ziemssen, Z. Wang, M. Dong, S. Schnichels, T. Qiu, and P. Fischer, Sci. Adv. **4**(11), eaat4388 (2018).
[2]A. Ghosh and P. Fischer, Nano Lett. **9**(6), 2243–2245 (2009).
[3]J. Giltinan and M. Sitti, IEEE Robot. Autom. Lett. **4**(2), 508–514 (2019).
[4]S. Tottori, L. Zhang, F. Qiu, K. K. Krawczyk, A. Franco-Obregón, and B. J. Nelson, Adv. Mater. **24**(6), 811–816 (2012).
[5]B. Wang, K. F. Chan, J. Yu, Q. Wang, L. Yang, P. W. Y. Chiu, and L. Zhang, Adv. Funct. Mater. **28**, 1705701 (2018).
[6]J. Cui, T.-Y. Huang, Z. Luo, P. Testa, H. Gu, X.-Z. Chen, B. J. Nelson, and L. J. Heyderman, Nature **575**(7781), 164–168 (2019).
[7]T. Li, J. Li, K. I. Morozov, Z. Wu, T. Xu, I. Rozen, A. M. Leshansky, L. Li, and J. Wang, Nano Lett. **17**(8), 5092–5098 (2017).
[8]Y. Alapan, U. Bozuyuk, P. Erkoc, A. C. Karacakol, and M. Sitti, Sci. Robot. **5**(42), eaba5726 (2020).
[9]H. Zhang, Z. Li, C. Gao, X. Fan, Y. Pang, T. Li, Z. Wu, H. Xie, and Q. He, Sci. Robot. **6**, eaaz9519 (2021).
[10]B. Wang, K. F. Chan, K. Yuan, Q. Wang, X. Xia, L. Yang, H. Ko, Y.-X. J. Wang, J. J. Y. Sung, and P. W. Y. Chiu, Sci. Robot. **6**(52), eabd2813 (2021).
[11]M. Pal, N. Somalwar, A. Singh, R. Bhat, S. M. Eswarappa, D. K. Saini, and A. Ghosh, Adv. Mater. **30**(22), 1800429 (2018).
[12]J. Guo, Z. Liang, Y. Huang, K. Kim, P. Vandeventer, and D. Fan, ACS Nano **14**(11), 15204–15215 (2020).
[13]K. Kim, X. Xu, J. Guo, and D. Fan, Nat. Commun. **5**, 3632 (2014).
[14]U. Ohiri, C. W. Shields, K. Han, T. Tyler, O. D. Velev, and N. Jokerst, Nat. Commun. **9**(1), 1791 (2018).
[15]D. Fan, Z. Yin, R. Cheong, F. Q. Zhu, R. C. Cammarata, C. Chien, and A. Levchenko, Nat. Nanotechnol. **5**(7), 545–551 (2010).
[16]L. Wang and Q. Li, Chem. Soc. Rev. **47**(3), 1044–1097 (2018).
[17]R. Dong, Y. Cai, Y. Yang, W. Gao, and B. Ren, Acc. Chem. Res. **51**(9), 1940–1947 (2018).
[18]L. Ren, W. Wang, and T. E. Mallouk, Acc. Chem. Res. **51**(9), 1948–1956 (2018).
[19]L. Ren, D. Zhou, Z. Mao, P. Xu, T. J. Huang, and T. E. Mallouk, ACS Nano **11**(10), 10591–10598 (2017).
[20]W. Wang, W. Duan, Z. Zhang, M. Sun, A. Sen, and T. E. Mallouk, Chem. Commun. **51**(6), 1020–1023 (2015).
[21]G.-Z. Yang, P. Fischer, and B. Nelson, Sci. Robot. **2**(10), eaap9294 (2017).
[22]Z. Liang and D. Fan, Sci. Adv. **4**(9), eaau0981 (2018).
[23]Z. Liang, D. Teal, and D. Fan, Nat. Commun. **10**(1), 1 (2019).
[24]D. Fan, R. Cammarata, and C. Chien, Appl. Phys. Lett. **92**(9), 093115 (2008).
[25]Y. Huang, Z. Liang, M. Alsoraya, J. Guo, and D. Fan, Adv. Intell. Syst. **2**(7), 1900127 (2020).
[26]T. B. Jones and T. B. Jones, *Electromechanics of Particles* (Cambridge University Press, 2005).
[27]J. D. Jackson, *Classical Electrodynamics* (John Wiley & Sons, 2007).
[28]M. Z. Bazant and T. M. Squires, Phys. Rev. Lett. **92**(6), 066101 (2004).
[29]P. García-Sánchez, J. E. Flores-Mena, and A. Ramos, Micromachines **10**(2), 100 (2019).
[30]T. Miloh, "Nonlinear alternating electric field dipolophoresis of spherical nanoparticles," Phys. Fluids **21**(7), 072002 (2009).
[31]J. Flores-Mena, P. García-Sánchez, and A. Ramos, Phys. Rev. E **99**(3), 032603 (2019).
[32]L. Rodríguez-Sánchez, A. Ramos, and P. García-Sánchez, Phys. Rev. E **100**(4), 042616 (2019).
[33]H. Zhou, M. A. Preston, R. D. Tilton, and L. R. White, J. Colloid Interface Sci. **285**(2), 845–856 (2005).
[34]W. Cao, M. Chern, A. M. Dennis, and K. A. Brown, Nano Lett. **19**(8), 5762–5768 (2019).